PNAS RESEARCH ARTICLE | NEUROSCIENCE OPEN ACCESS

Inhibition of connexin hemichannels alleviates neuroinflammation and hyperexcitability in temporal lobe epilepsy

Anni Guo[a,b], Huiqi Zhang[a,b], Huanhuan Li[a,b], Arthur Chiu[a,b], Claudia García-Rodríguez[c], Carlos F. Lagos[d], Juan C. Sáez[c,1], and Chunyue Geoffrey Lau[a,b,1]

Contributed by Juan C. Sáez; received August 1, 2022; accepted October 4, 2022; reviewed by John O'Brien and Jean Jiang

Temporal lobe epilepsy (TLE) is one of the most common types of epilepsy, yet approximately one-third of patients are refractory to current anticonvulsive drugs, which target neurons and synapses. Astrocytic and microglial dysfunction is commonly found in epileptic foci and has been shown to contribute to neuroinflammation and hyperexcitability in chronic epilepsy. Accumulating evidence points to a key role for glial hemichannels in epilepsy, but inhibiting both connexin (Cx) gap junctions and hemichannels can lead to undesirable side effects because the former coordinate physiological functions of cell assemblies. It would be a great benefit to use an orally available small molecule to block hemichannels to alleviate epileptic symptoms. Here, we explored the effect of D4, a newly developed compound that inhibits the Cx hemichannels but not Cx gap junctions using the pilocarpine mouse model of TLE. In vitro application of D4 caused a near-complete reduction in the pilocarpine-induced cell membrane permeability associated with increased Cx hemichannel activity. Moreover, preadministration of D4 in vivo effectively reduced neuroinflammation and altered synaptic inhibition, which then enhanced the animal survival rate. Posttreatment with a single dose of D4 in vivo has prolonged effects on suppressing the activation of astrocytes and microglia and rescued the changes in neuroinflammatory and synaptic gene expression induced by pilocarpine. Collectively, these results indicate that targeting Cx hemichannels by D4 is an effective and promising strategy for treating epilepsy in which neuroinflammation plays a critical role.

seizure | antiepileptic drug | connexon | excitability

Significance

Although symptomatic medications are available, many temporal lobe epilepsy (TLE) patients remain unresponsive to treatment and new drug targets are needed. Connexin-based gap junctions and hemichannels in brain glial cells are implicated in TLE, but blocking gap junctions can lead to undesirable side effects. Here, we studied the effect of a small organic molecule called D4, which selectively blocks connexin hemichannels, and tested its efficacy in treating TLE using a mouse model. In vivo application of D4 strongly suppresses TLE-induced hemichannel activity and neuroinflammation, curbs TLE seizures, and increases the survival rate. Thus, targeted blockade of brain connexin hemichannels with D4 is a potentially effective strategy to treat TLE symptoms and neuropathology.

Epilepsy is one of the most prevalent chronic brain disorders and is characterized by recurrent and spontaneous seizures. Seizures are highly synchronized neuronal discharges that arise from some epileptogenic regions and can spread to large areas in the brain. While about 50 million people worldwide are suffering from epilepsy, almost one-third of patients are resistant to available antiepileptic drugs, which mainly target synapses or neurons (1). With such refractory rates, the discovery of new pharmacological targets is important for providing better treatment.

Accumulating evidence has shown that the pathology of epilepsy involves the interaction between neurons and glia. Astrocytes have tight connections with neurons both morphologically and physiologically at the tripartite synapse, which consists of the pre- and postsynaptic elements, and astrocytic processes (2), modulating neural activity through the uptake or release of transmitters (3). Astrocytes undergo changes in morphology, biochemistry, and physiology in response to brain insults (4). Reactive astrogliosis is known to be present in epileptic foci exhibiting extensive physiological and molecular changes such as ion and neurotransmitter homeostasis disruption and changes in transporter and enzyme systems (3, 5), which further exacerbate neuronal hyperexcitability and epileptic seizures (6–8).

Connexins (Cxs) are transmembrane proteins which span the cell membrane four times with N and C terminals located intracellularly (9). Cx proteins build two different channel types: hemichannels (HCs) and gap junction channels (GJCs) (9–11). Six Cx isoforms make up an HC with an aqueous pore in the center. They are expressed on the nonapposed cell membrane and connect the cytosol and extracellular environment (9–11). HC opening facilitates the passage of ions and molecules including metabolites and cell-signaling molecules (11, 12). GJCs are formed from two HCs on two adjacent cells docking with each other, and their permeability features permit the coordination of electrical and metabolic responses (13). In the brain, 12 subtypes of Cxs are expressed and the most abundant one is Cx43, which is dominantly expressed in astrocytes and, to a lesser extent, in activated microglia (14). The open probability of Cx HCs is low under resting conditions but may increase transiently under specific

Author contributions: J.C.S. and C.G.L. designed research; A.G., H.Z., H.L., A.C., C.G.-R., and C.F.L. performed research; J.C.S. and C.G.L. contributed new reagents/analytic tools; A.G., H.Z., H.L., A.C., C.G.-R., C.F.L., J.C.S., and C.G.L. analyzed data; and A.G., H.Z., H.L., A.C., C.G.-R., C.F.L., J.C.S., and C.G.L. wrote the paper.

Reviewers: J.J., The University of Texas Health Science Center at San Antonio; and J.O., University of Houston College of Optometry.

The authors declare no competing interest.

[1]To whom correspondence may be addressed. Email: juancarlos.saez@uv.cl.

This article contains supporting information online at http://www.pnas.org/lookup/suppl/doi:10.1073/pnas.2213162119/-/DCSupplemental.

Published November 2, 2022.

physiological conditions without compromising the cell viability (11). Under pathological conditions, Cx HC opening can be altered by ischemia (15, 16), changes in redox status (17), phosphorylation status (18), or increased membrane expression (19, 20). Uncontrolled HC opening facilitates the excessive release of chemically active molecules such as glutamate, ATP, and D-serine, which can be toxic to the central nervous system (CNS) (21–28). This condition promotes deleterious outcomes, which have been shown in epilepsy, ischemia, and other neurodegenerative diseases (25–28). However, whether pharmacologically targeting glial Cx HCs is a promising avenue for epilepsy treatment is unclear.

In a recent study, we screened and identified a Cx HC inhibitor, a small organic molecule called D4, which has been shown to be effective in reducing pathological muscular atrophy (29). To explore the role of Cx HCs in epilepsy, we used D4 to block Cx HCs in the pilocarpine model of human temporal lobe epilepsy (TLE). While activation of astrocytes and microglia, as well as altered neuronal inhibition, are observed in a latent period after status epilepticus (SE), preapplication of D4 by oral gavage strongly reduced epilepsy-related neuroinflammation, altered synaptic inhibition, and enhanced the animal survival rate. Moreover, postepileptic treatment of D4 afforded robust normalization of glial cell activation, gene expression of neuroinflammatory and synaptic proteins, and glial HC activity in epileptic mice.

Results

Application of D4 Prepilocarpine Reduces TLE-Induced Neuroinflammation. To determine the contribution of Cx HCs in TLE-mediated neuroinflammation, we used the pilocarpine model of epilepsy in mice, a well-known model to produce phenotypes that resemble human TLE (30). We administered D4 (10 to 20 mg/kg, orally [p.o.]) 6 h before inducing SE using one dose of pilocarpine (200 to 300 mg/kg, intraperitoneally [i.p.]), and 7 d later we fixed the brains to examine the astrocytes and microglia (Fig. 1*A*). We first observed that preadministration of D4 increased the animals' 7-d survival rate after SE from 46 to 74% ($P = 0.049$; Fig. 1*B*). To broadly examine for neuroinflammation, we then evaluated the immunoreactivity of the cytoskeletal protein GFAP in astrocytes and calcium-binding protein Iba1 in microglia in the anterior piriform cortex (APC) and two subregions of the hippocampus, CA1 and dentate gyrus (DG). Pilocarpine treatment significantly up-regulated the covered area of GFAP protein reactivity in all regions (Fig. 1 *C* and *D*) with a higher $GFAP^+$ intensity in CA1 and DG (Fig. 1*C* and *SI Appendix*, Fig. S1*A*), reflecting an increased number of activated astrocytes (31). Preadministration of D4 reduced astrocyte activation as indicated by a reduced area covered by GFAP reactivity in APC (Fig. 1 *C* and *D*), but not in CA1 or DG (Fig. 1 *C* and *D* and *SI Appendix*, Fig. S1*A*). Similarly, pilocarpine treatment significantly up-regulated the covered area of Iba1 protein reactivity (Fig. 1 *E* and *F*) and $Iba1^+$ intensity (Fig. 1*E* and *SI Appendix*, Fig. S1*B*). Preapplication of D4 reduced microglia activation as indicated by the lower Iba1 reactivity and intensity in CA1 and DG as compared to D4-untreated animals (Fig. 1 *E* and *F* and *SI Appendix*, Fig. S1*B*). Overall, these results suggested that preadministration of D4 reduced TLE-mediated neuroinflammation.

Posttreatment of D4 Reverts the Activation of Astrocytes and Microglia in TLE. We showed that pretreatment with D4 reduces neuroinflammation mediated by TLE, but a postinsult treatment regimen would be more therapeutically beneficial. To examine whether post-SE D4 treatment could rescue TLE-mediated neuroinflammation, we administered one dose of D4 (5 to 10 mg/kg, p.o.) 5 h after pilocarpine injection (200 to 300 mg/kg, i.p.), and 7 d later we fixed the brains to examine the astrocytes and microglia (Fig. 1*A*). Posttreatment of D4 reverted the pilocarpine-induced astrocyte activation as indicated by a smaller area covered with GFAP reactivity in APC, CA1, and DG (Fig. 1 *C* and *D*). Besides astrocytes, posttreatment with D4 also reverted the microglia activation induced by pilocarpine as indicated by the reduced covered area of Iba1 reactivity and fluorescence intensity in APC, CA1, and DG (Fig. 1 *E* and *F* and *SI Appendix*, Fig. S1*B*). Overall, these results suggested that posttreatment with D4 strongly alleviated TLE-mediated neuroinflammation with long-term effects.

Application of D4 Prepilocarpine Ameliorates the Altered Synaptic Inhibition in the Epileptic Hippocampus. We assayed for the effects of D4 on neuropathology in TLE. To assess the effects of D4 and TLE on neuronal excitability, we performed two experiments. First, we performed whole-cell patch clamp to record spontaneous inhibitory postsynaptic currents (sIPSCs) of pyramidal neurons in the hippocampal CA1. We used the same experimental scheme as above and applied D4 6 h before the single dose of pilocarpine and performed electrophysiological recording 3 d later (Fig. 2*A*). Pilocarpine decreased the amplitude and frequency (Fig. 2 *C1* and *C2*) of sIPSCs in CA1 pyramidal neurons. While pretreatment of D4 did not alter the pilocarpine-induced decrease in sIPSC amplitude (Fig. 2 *C1*), it completely reverted the decrease in sIPSC frequency (Fig. 2 *C2*). These results suggested that preapplication of D4 ameliorated the altered synaptic inhibition in the epileptic brain.

D4 Rapidly Attenuates Electrographic Seizures In Vivo. Next, to determine if D4 can curb electrographic seizures, we performed local field potential (LFP) recordings in the primary motor cortex of anesthetized mice. We first induced SE by injection of pilocarpine (200 to 250 mg/kg, i.p.) into awake mice. After mice were anesthetized, a 30-min recording was made once before (control) and after application of D4 (Fig. 2*D*). Recording during SE has two advantages. First, the epileptic spikes are stably expressed and can last for at least an hour, providing a good window to test the effect of drugs in the same animal. Second, anesthesia during this stage has a lower mortality rate than anesthesia before pilocarpine injection. We first measured the effects of vehicle (oral gavage) on the power, number, and amplitude of epileptic spikes. These parameters were high before and during vehicle administration, suggesting that vehicle has no detectable effect on seizure activity (*SI Appendix*, Fig. S2). By contrast, D4 treatment largely attenuated electrographic seizure activities, as indicated by the raw LFP traces and energy spectrogram (Fig. 2*E*). Power spectral analysis indicated that D4 had a stronger effect on the power of low-frequency bands compared to high-frequency bands (Fig. 2*F*). Additionally, D4 significantly reduced the number of epileptic spikes and the fraction of high-amplitude spikes (Fig. 2 *G* and *H*). These results suggest that D4 shows potent and rapid antiseizure effects.

Posttreatment with D4 Reverts the Changes in Messenger RNA Levels of Neuroinflammatory and Synaptic Genes in TLE. Our data thus far revealed that D4 could afford robust reduction of neuroinflammation and seizure symptoms, but the underlying molecular events were unclear. To determine the temporal profile

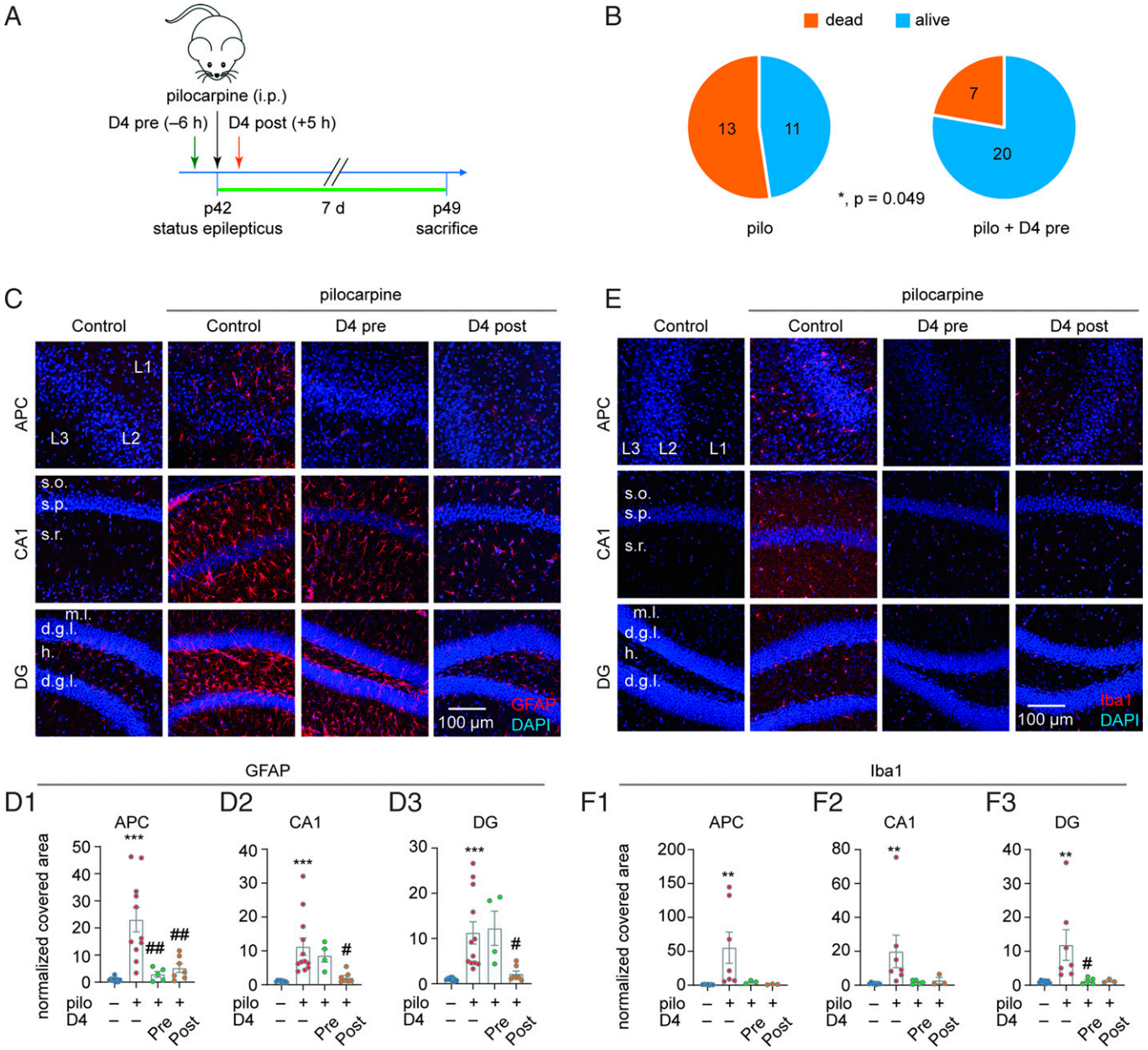

Fig. 1. D4 treatment decreases activation of astrocytes and microglia in TLE. (*A*) Timeline of experiment. SE was induced in P42 wild-type mice by intraperitoneal injection of pilocarpine (200 to 300 mg/kg), and D4 was applied by oral gavage 6 h (10 to 20 mg/kg) before or 5 h (5 to 10 mg/kg) after pilocarpine injection. Seven days after status epilepticus, mice were killed for immunostaining. (*B*) Quantification of animal survival rate in pilocarpine and pilocarpine with D4 pretreatment within 7 d after pilocarpine injection. (*Left*: 45.8%, $n = 24$; *Right*: 74.1%, $n = 27$, $P = 0.049$, Fisher's exact test). (*C*) Representative images of GFAP expression in APC, CA1, and DG under four experimental conditions: ctrl; pilo; pilo + D4 (pre); pilo + D4 (post). (*D*) Quantification of GFAP relative area of GFAP expression percentage in APC (ctrl: 1.0 ± 0.26, $n = 9$; pilo: 23.1 ± 4.5, $n = 11$, $P < 0.001$; pilo + D4 pre: 2.9 ± 1.1, $n = 5$, $P = 0.002$; pilo + D4 post: 5.2 ± 1.6, $n = 7$, $P = 0.002$) (D1), CA1 (ctrl: 1.0 ± 0.1, $n = 9$; pilo: 11.2 ± 2.6, $n = 12$, $P < 0.001$; pilo + D4 pre: 8.6 ± 1.9, $n = 4$, $P = 1.000$; pilo + D4 post: 2.1 ± 0.6, $n = 7$, $P = 0.02$) (D2), and DG (ctrl: 1.0 ± 0.11, $n = 9$; pilo: 11.3 ± 2.5, $n = 12$, $P < 0.001$; pilo + D4 pre: 12.3 ± 3.8, $n = 4$, $P = 1.000$; pilo + D4 post: 2.2 ± 0.6, $n = 7$, $P = 0.04$) (D3). (*E*) Representative images of Iba1 expression in APC, CA1, and DG under four experimental conditions: ctrl; pilo; pilo + D4 pre; pilo + D4 post. (*F*) Quantification of Iba1 relative area of Iba1 expression percentage in APC (ctrl: 1.0 ± 0.2, $n = 7$; pilo: 55.4 ± 23.0, $n = 7$, $P = 0.002$; pilo + D4 pre: 4.77 ± 1.46, $n = 3$; pilo + D4 post: 1.3 ± 0.4, $n = 3$, $P = 0.066$) (F1), CA1 (ctrl: 1.0 ± 0.18, $n = 7$; pilo: 20.0 ± 9.6, $n = 7$, $P = 0.006$; pilo + D4 pre: 1.7 ± 0.5, $n = 5$, $P = 0.08$; pilo + D4 post: 2.8 ± 1.9, $n = 3$, $P = 0.36$) (F2), and DG (ctrl: 1.0 ± 0.16, $n = 7$; pilo: 11.9 ± 4.5, $n = 7$, $P = 0.006$; pilo + D4 pre: 1.2 ± 0.4, $n = 5$, $P = 0.02$; pilo + D4 post: 1.2 ± 0.3, $n = 3$, $P = 0.186$) (F3). $^{***}P < 0.001$, $^{**}P < 0.01$: significant increase compared with ctrl; $^{\#\#}P < 0.01$, $^{\#}P < 0.05$: significant decrease compared with pilo. One-way ANOVA followed by Tukey's multiple comparisons post hoc test was used to compare GFAP normalized covered area in APC. Independent-samples Kruskal–Wallis test (significance values were adjusted by the Bonferroni correction) was used to compare GFAP normalized covered area in CA1 and DG and Iba1 normalized covered area in APC, CA1, and DG. Fisher's exact test was used for the animal survival number dataset. (All staining data are normalized to the corresponding control group.)

of neuroinflammatory and synaptic gene expression after SE, we examined the changes in the amount of messenger RNA (mRNA) at different time points by qRT-PCR. Measurements were performed at 1 d, 3 d, or 7 d after inducing SE in the APC and hippocampus (*SI Appendix*, Fig. S3*A*). Among the different time points tested, we found that mRNA of inflammatory mediators was most significantly increased in the hippocampus at 3 d after SE, including genes related to astrocyte activation (*gfap*), microglia activation (*cd68*, *trem2*, *cx3cr1*, *tlr9*), and immune response such as complement system (*c3*), inflammasome (*nlrp3*), and inflammatory pathway (*Tnf*, *Tnfr1*) (*SI Appendix*, Fig. S3*C*). mRNA levels of synaptic elements (*Gad1*, *vglut1*,

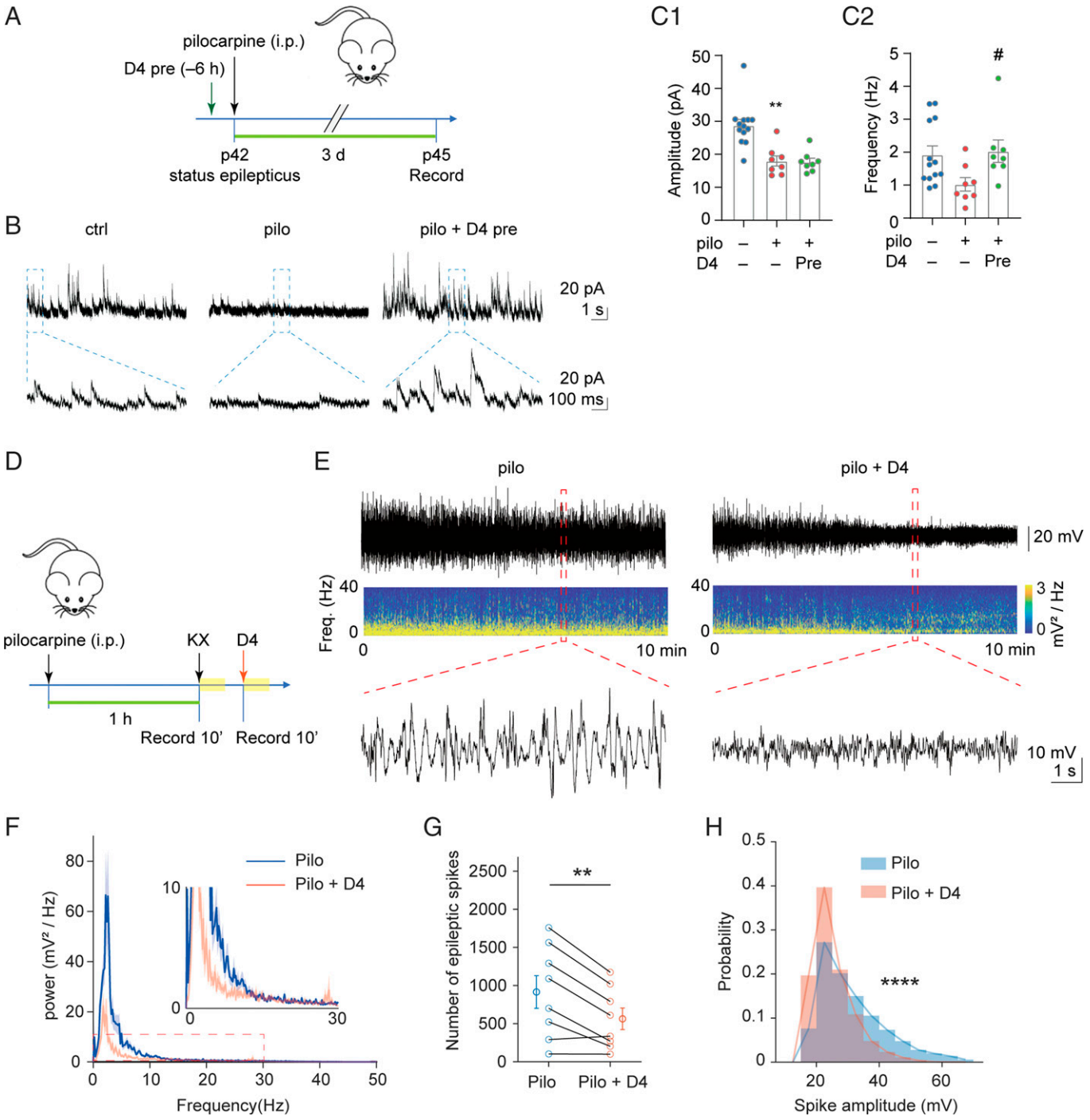

Fig. 2. D4 attenuates altered synaptic inhibition and electrographic seizures. (*A*) Timeline of whole-cell patch-clamp recording. SE was induced in P42 wild-type mice by intraperitoneal injection of pilocarpine (200 to 300 mg/kg), D4 was administered by gavage 6 h (10 to 20 mg/kg) before pilocarpine injection. Three days after SE, mice were killed for further whole-cell patch-clamp recording. (*B*) Representative trace of sIPSCs in CA1 pyramidal neurons within 10 s (*Above*) and 1s (*Below*) scale. (*C*) Quantification of mean amplitude (ctrl: 28.8 ± 1.8 pA, $n = 13$; pilo: 18.0 ± 1.6 pA, $n = 8$, $P = 0.002$; pilo + D4 pre: 17.7 ± 1.1 pA, $n = 8$, $P = 1.000$) (C1) and frequency (ctrl: 1.9 ± 0.3 Hz, $n = 13$; pilo: 1.02 ± 0.20 Hz, $n = 8$, $P = 0.08$; pilo + D4 pre: 2.03 ± 0.34 Hz, $n = 8$, $P = 0.035$) (C2) of sIPSCs in CA1 pyramidal neurons. $^{**}P < 0.01$: significant decrease compared with ctrl; $^{\#}P < 0.05$: significant increase compared with pilo. Independent-samples Kruskal–Wallis test (significance values were adjusted by the Bonferroni correction). (*D*) Scheme of experiment for D4 treatment in pilocarpine induced acute epileptic mice. First arrow denotes p42, status epilepticus. The yellow blocks represent the recording period. (*E*) Representative raw LFP and LFP spectrogram during pilocarpine induced SE in pilocarpine group and pilocarpine with D4 group. Below are enlarged raw LFP segments corresponding to the red dotted boxes. (*F*) Power spectral analysis of pilocarpine group and pilocarpine with D4 group. Thick dark lines indicate mean and shaded light-colored areas indicate SEM. (*G*) Effect of D4 on the number of epileptic spikes during 10-min recording. Paired *t* test, $^{**}P < 0.01$. (*H*) D4 reduced the amplitude of epileptic spikes (rank-sum test, $^{****}P < 0.0001$) and altered their distribution shapes (two-sample Kolmogorov–Smirnov test, $^{****}P < 0.0001$).

homer1, *pvalb*) were generally decreased in the hippocampus 3 d after SE (*SI Appendix*, Fig. S3*B*). In APC, mRNA levels showed a similar trend that neuroinflammation and reduction of synaptic elements reached maximum 3 d after SE (*SI Appendix*, Fig. S4 *A* and *B*). Furthermore, Cx43 mRNA level did not show significant change on 1, 3, or 7 d after pilocarpine injection in the APC (*SI Appendix*, Fig. S3*B*) and hippocampus (*SI Appendix*, Fig. S4*A*). Although Cx43 mRNA level indicates expression of both Cx43 HCs and GJCs, these results may suggest that Cx HCs increased opening probability but not expression in response to brain insults.

Understanding that changes in mRNA levels generally peaked at 3 d after SE, we next tested whether D4 could revert these changes. We administered one dose (+5 h) or three doses (+5 h, +1 d, +3 d) of D4 after pilocarpine injection and repeated the qRT-PCR experiments (Fig. 3*A*). While one dose of D4 after pilocarpine offered modest but nonsignificant effects on the amount of mRNAs in APC and hippocampus (*SI Appendix*, Fig. S5*A* and Fig. 3*B*), three doses of D4 significantly increased the mRNA amount for *Gad1*, *homer1*, and *pvalb* (*SI Appendix*, Fig. S5*A* and Fig. 3*B*). D4 had a slightly stronger effect on mRNA levels of neuroinflammation molecules after SE in that both one dose and three doses of D4 treatment suppressed their increase. One dose of D4 treatment significantly decreased the mRNA levels of several molecular markers of neuroinflammation in APC (*Tnf*, *tlr9*; *SI Appendix*, Fig. S5*B*) and hippocampus (*Tnf*, *nlrp3*; see Fig. 5*C*). Moreover, three doses of D4 treatment after pilocarpine injection significantly reduced the mRNA levels of neuroinflammation markers (*gfap*, *cd68*, *trem2*, *cx3cr1*, *tlr9*, *c3*, *nlrp3*, *Tnf*, *Tnfr1*; *SI Appendix*, Fig. S4*B* and see Fig. 5*C*). Overall, these results suggested that posttreatment with D4 reverts the levels of mRNA of proteins involved in neuroinflammation and synapse function induced by SE.

D4 Inhibits the Pilocarpine-Induced Astrocytic HC Activity in Acute Slices. Our previous results showed that D4 reduces TLE-mediated neuroinflammation and hyperexcitability and posttreatment with D4 has prolonged effects on reverting glia activation and alteration in mRNA profile induced by pilocarpine. To explore how D4 could alleviate the increased uptake of extracellular small molecules induced by pilocarpine, we applied D4 in acute slice of epileptic mice and measured overall carboxyfluorescein (CBF) uptake in GFAP-positive cells. We first examined CBF uptake in acute slice of saline-injected mice oxygenated in ACSF (artificial cerebrospinal fluid) or DCFS (divalent cation-free solution, Ca^{2+} and Mg^{2+} excluded from ACSF) (Fig. 4*B*), a condition known to increase the open probability of Cx HCs (11). While CBF uptake in regular ACSF was very weak, CBF uptake in DCFS was dramatically increased, as indicated by overall CBF area percentage and mean intensity in healthy APC (*SI Appendix*, Fig. S6 *A* and *B*), CA1 (*SI Appendix*, Fig. S7 *A* and *B*), and DG (Fig. 4 *C* and *D*).

We next measured CBF uptake in acute slice of mice injected with one dose of pilocarpine and performed a dye uptake experiment 3 or 7 d postpilocarpine (p3 or p7; Fig. 4*A*). D4 was applied in vivo (p7 + D4 in vivo) or in vitro (p3 + D4 or p7 + D4). For the in vitro experiments, freshly obtained brain slices from epileptic mice were first incubated with

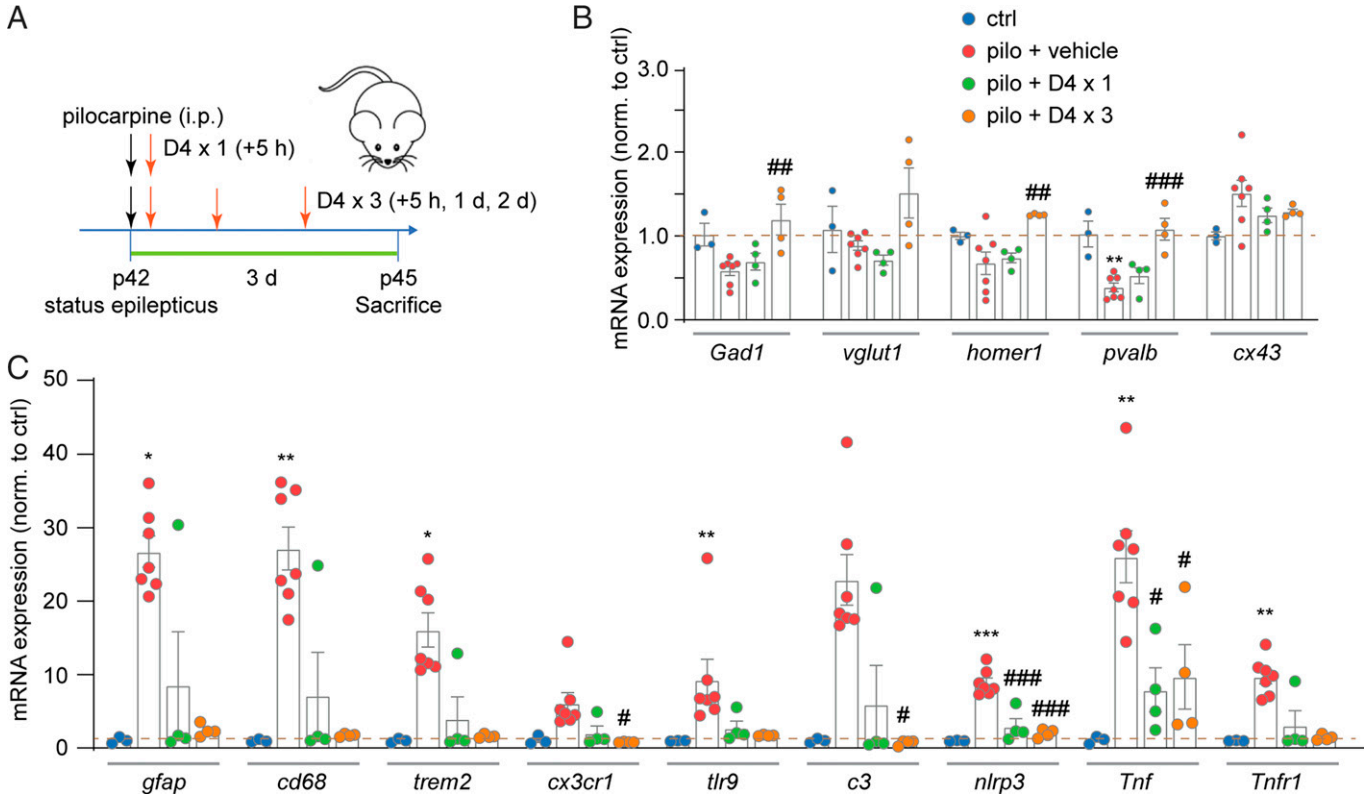

Fig. 3. Treatment with D4 after SE rescues the altered mRNA levels of neuroinflammatory and synaptic proteins in the hippocampus. (*A*) Timeline of experiment. SE was induced in P42 wild-type mice by intraperitoneal injection of pilocarpine (200 to 300 mg/kg), and D4 was applied by oral gavage once at 5 h (5 to 10 mg/kg) or three times at 5 h, 1 d, and 2 d (5 to 10 mg/kg) after pilocarpine injection. Three days after SE, mice were killed for tissue extraction and further quantitative real-time PCR. (*B*) Relative mRNA expression of *Gad1*, *vglut1*, *homer1*, *pvalb*, and *cx43* in four groups: ctrl; pilo; pilo + D4 × 1 (+5h); pilo + D4 × 3 (+5 h, +1 d, +2 d) in hippocampus. Fold change is normalized to control group. (*C*) Relative mRNA expression of *gfap*, *cd68*, *trem2*, *cx3cr1*, *tlr9*, *c3*, *nlrp3*, *Tnf*, and *Tnfr1* in four groups: ctrl; pilo; pilo + D4 × 1 (+5 h); pilo + D4 × 3 (+5 h, +1 d, +2 d) in hippocampus. Fold change is normalized to control group. $^{***}P < 0.001$, $^{**}P < 0.01$, $^{*}P < 0.05$: significant increase/decrease compared with ctrl; $^{###}P < 0.001$, $^{##}P < 0.01$, $^{#}P < 0.05$: significant increase/decrease compared with pilo. One-way ANOVA followed by Tukey's multiple comparisons post hoc test was used to compare expression of *Gad1*, *vglut1*, *homer1*, *pvalb*, *cx43*, *nlrp3*, and *Tnf* among four groups; independent-samples Kruskal–Wallis test (significance values were adjusted by the Bonferroni correction) was used to compare expression of *gfap*, *cd68*, *trem2*, *cx3cr1*, *tlr9*, *c3*, and *Tnfr1* among four groups. pilo + D4 × 1 (+5 h): (*Gad1*: 0.69 ± 0.10, $n = 4$, $P = 0.886$; *vglut1*: 0.71 ± 0.06, $n = 4$, $P = 0.853$; *homer1*: 0.74 ± 0.06, $n = 4$, $P = 0.974$; *pvalb*: 0.53 ± 0.09, $n = 4$, $P = 0.691$; *Tnf*: 8.0 ± 3.0, $n = 4$, $P = 0.012$; *nlrp3*: 3.0 ± 1.1, $n = 4$, $P < 0.001$). pilo + D4 × 3 (+5 h, +1 d, +2 d): (*Gad1*: 1.20 ± 0.18, $n = 4$, $P = 0.005$; *homer1*: 1.25 ± 0.01, $n = 4$, $P = 0.009$; *pvalb*: 1.08 ± 0.13, $n = 4$, $P < 0.001$; *gfap*: 2.4 ± 0.4, $n = 4$, $P = 0.428$; *cd68*: 1.8 ± 0.1, $n = 4$, $P = 0.389$; *trem2*: 1.6 ± 0.1, $n = 4$, $P = 0.459$; *cx3cr1*: 0.83 ± 0.03, $n = 4$, $P = 0.011$; *tlr9*: 1.72 ± 0.05, $n = 4$, $P = 0.104$; *c3*: 0.75 ± 0.10, $n = 4$, $P = 0.042$; *nlrp3*: 2.0 ± 0.3, $n = 4$, $P < 0.001$; *Tnf*: 9.7 ± 4.4, $n = 4$, $P = 0.023$; *Tnfr1*: 1.4 ± 0.2, $n = 4$, $P = 0.297$).

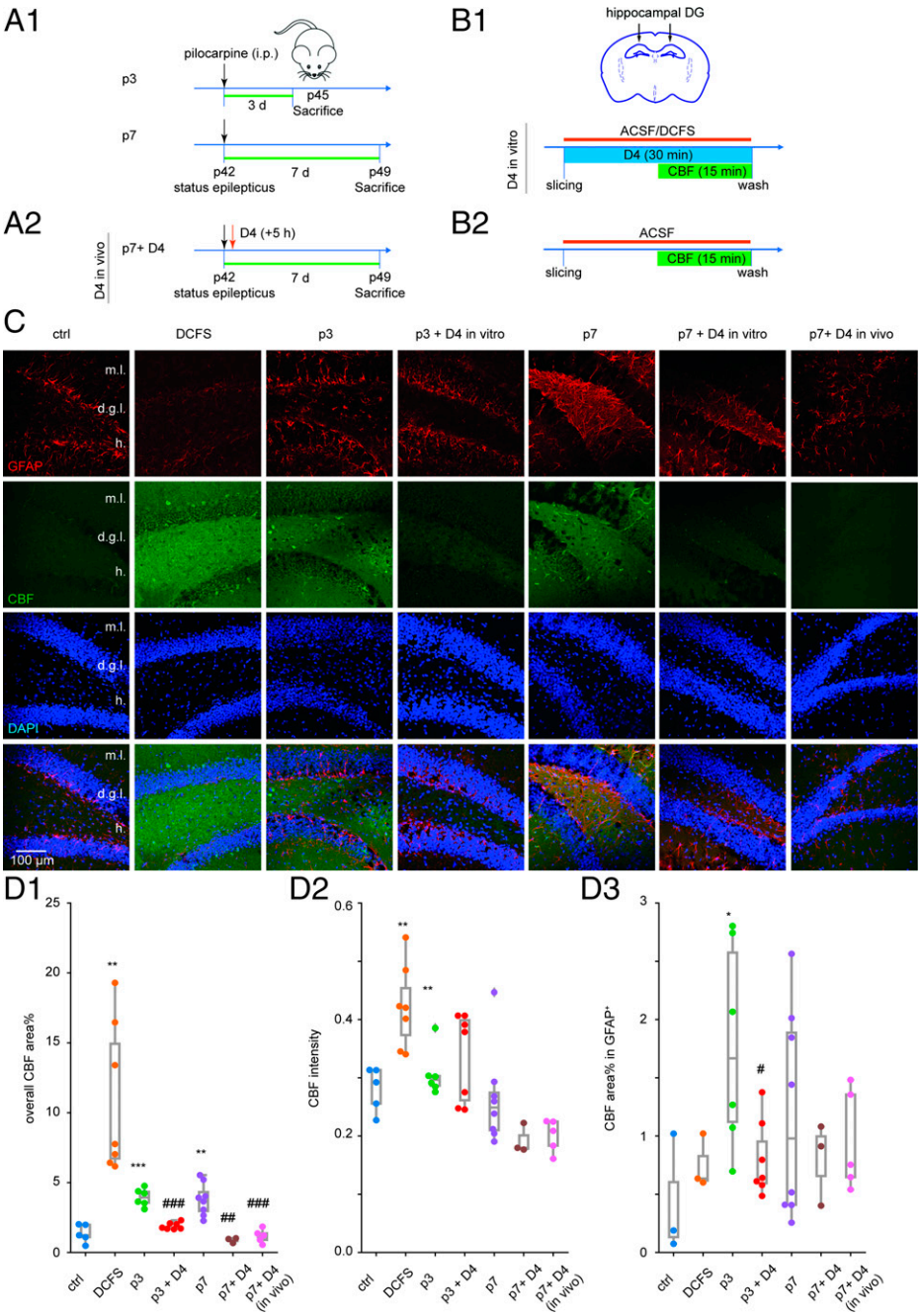

Fig. 4. D4 in vitro or in vivo inhibits pilocarpine-induced astrocytic HC activity in hippocampal slices. (*A*) Timeline of experiment. SE was induced in P42 wild-type mice by intraperitoneal injection of pilocarpine (200 to 300 mg/kg) For D4 in vitro experiment, 3 or 7 d after SE, mice were killed for acute slicing and further dye uptake experiment (*A1*). For D4 in vivo experiment, D4 was applied by oral gavage once at 5 h (10 mg/kg) after pilocarpine injection (*A2*). (*B*) Timeline of dye uptake experiment. Acute brain slices were obtained from mice 3 or 7 d after pilocarpine injection. Acute slices were incubated in a chamber oxygenated by bubbling gas mixture (95% O_2 and 5% CO_2) into ACSF solution (or DCFS in the positive control group). D4 (10 μM) was applied in ACSF all the time for 30 min. CBF was added 15 min after D4. Fifteen minutes after CBF application, slices were washed in ACSF to stop dye uptake (*B1*). For slices subjected to D4 in vivo previously, they were incubated in ACSF without D4 in vitro (*B2*). (*C*) Representative images showing GFAP (red) and CBF (green) uptake of acute hippocampal slices from control mice (ctrl: slices incubated in ACSF; DCFS: slices incubated in DCFS) and pilocarpine-injected mice (p3: 3 d after SE; p3 + D4: 3 d SE, slices treated with D4; p7: 7 d after SE; p7 + D4: 7 d SE, slices treated with D4; p7 + D4 in vivo: 7 d after SE, D4 applied in vivo after pilocarpine injection). Images were taken from the DG zone. (*D*) Quantification of overall CBF area percentage (ctrl: 1.4 ± 0.3, n = 5; DCFS: 10.9 ± 2.0, n = 7, P = 0.003; p3: 3.9 ± 0.3, n = 6, P < 0.001; p3 + D4: 1.9 ± 0.1, n = 7, P < 0.001; p7: 3.8 ± 0.4, n = 8, P = 0.001; p7 + D4: 0.9 ± 0.1, n = 3, P = 0.001; p7 + D4 in vivo: 1.2 ± 0.2, n = 5, P < 0.001) (*D1*), CBF mean intensity (ctrl: 0.28 ± 0.02, n = 5; DCFS: 0.42 ± 0.03, n = 7, P = 0.003; p3: 0.31 ± 0.02, n = 6, P = 0.002) (*D2*), and CBF area percentage in $GFAP^+$ area (ctrl: 0.4 ± 0.3, n = 3; p3: 1.8 ± 0.4, n = 6, P = 0.025; p3 + D4: 0.8 ± 0.1, n = 7, P = 0.039) (*D3*). ***P < 0.001, **P < 0.01, *P < 0.05: significant decrease compared with ctrl; $^{###}P$ < 0.001, $^{##}P$ < 0.01, $^{#}P$ < 0.05: significant decrease compared with corresponding pilocarpine group (p3 + D4 compared with p3; p7 + D4 compared with p7). Independent-samples Kruskal–Wallis test (significance values were adjusted by the Bonferroni correction) was used to compare CBF mean intensity among three groups (ctrl, p3 and p3 + D4; ctrl, p7 and p7 + D4; ctrl, p7 and p7 + D4 in vivo). One-way ANOVA followed by Tukey's multiple comparisons post hoc test was used to compare overall CBF area percentage and CBF area percentage in the $GFAP^+$ area for the rest dataset among three groups (ctrl, p3 and p3 + D4; ctrl, p7 and p7 + D4; ctrl, p7 and p7 + D4 in vivo). Two-sided t test was used to compare overall CBF area percentage, CBF mean intensity, and CBF area percentage in the $GFAP^+$ area between the ctrl and DCFS group.

10 μM D4 or vehicle control for 30 min in ACSF saturated with oxygen, then 100 μM CBF was added to determine dye uptake (Fig. 4*B*). CBF uptake in epileptic mice 3 or 7 d after SE was dramatically increased, as indicated by overall CBF area percentage and mean of fluorescence intensity (*SI Appendix*, Figs. S6 *A* and *B* and S7 *A* and *B* and Fig. 4 *C* and *D*). Both

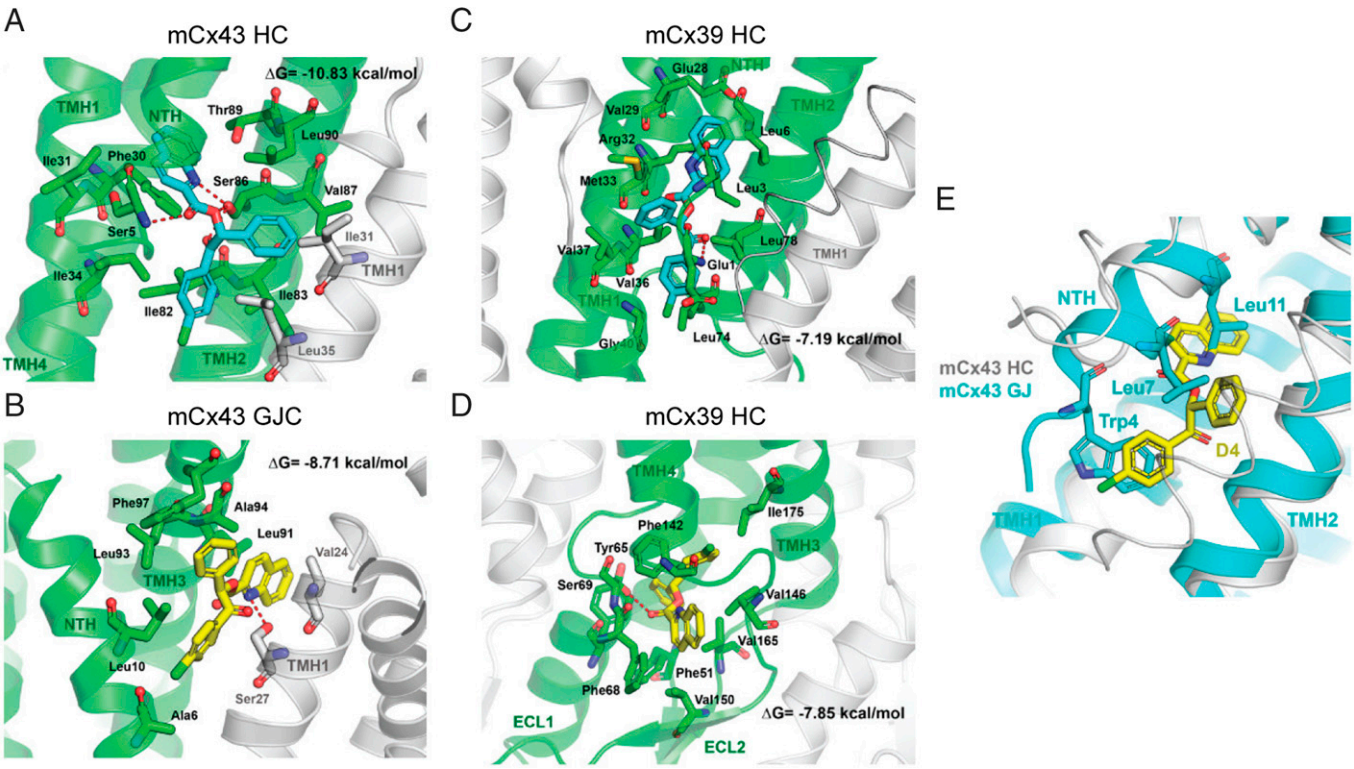

Fig. 5. Molecular modeling of mCx43 and mCx39 channels and their interactions with D4. D4 interactions with mCx43 HC (*A*), mCx43 gap junction (*B*), mCx39 within membrane plane binding site 1 (*C*), and extracellular binding site 2 (*D*). D4 is depicted with carbon atoms in cyan or yellow. The main Cx protomer with carbon atoms and ribbons is shown in green, while the adjacent protomers with carbons atoms and ribbons are depicted in white color. Hydrogen-bond interactions are depicted as red dashed lines. Superimposition of mCx43 HC with best docking results for D4 and mCx43 gap junction overlapping residues Trp4, Leu-7, and Leu11 (*E*). D4 is shown with carbon atoms in yellow, and residues in NTH of mCx43 in gap junction conformation are shown with carbon atoms in cyan.

incubation with D4 in vitro and application of D4 in vivo significantly decreased overall CBF area percentage in APC, CA1, and DG (*SI Appendix*, Figs. S6 *A* and *B* and S7 *A* and *B* and Fig. 4 *C* and *D*). To examine whether uptake in astrocytes was specifically modulated, we fixed the brain slices after CBF uptake and performed immunofluorescence staining for GFAP using a different color channel. CBF uptake in GFAP-positive cells was significantly increased in slices from epileptic mice in DG (Fig. 4*C*, D3), and this was dampened by incubation with D4 in vitro or in vivo (DG, Fig. 4*C*, D3; APC, *SI Appendix*, Fig. S6; CA1, *SI Appendix*, Fig. S7). Overall, these results suggested that Cx HC activity increases during epileptic activity, and this was inhibited by D4.

An In Silico Study Predicts that D4 Binds Preferentially to Cx43 HCs. We recently showed that D4 inhibits Cx43 HCs but neither Cx39 HCs nor Cx43 GJCs (29). Here, we also tested whether D4 can inhibit other Cx HC isoforms. In HeLa cells expressing either mCx26 or mCx30, dye uptake (DAPI) was strongly blocked by D4 (*SI Appendix*, Fig. S8). Since HCs formed by Cx26 or Cx30 can be coexpressed with Cx43 in certain brain regions (11), our results suggests that D4 can block all possible Cx HC expressed by astrocytes. However, a molecular and structural explanation for the selectivity, particularly between GJC vs. HC, is lacking. To identify the potential binding sites of D4 with Cx43 and Cx39, as a first step we constructed comparative models of mCx43 HC, mCx43 GJC, and mCx39 HC using the structure of Cx26 and Cx46 as templates. The mCx39 was modeled using the human Cx26 and ovine Cx46 as template with a 27.8% sequence identity and 52.7% sequence similarity. The mCx39 was modeled using the human Cx26 and ovine Cx46 as template with a 53.2% sequence identity and 72.7% sequence similarity (residues 122 to 139 were not modeled). The obtained models were validated in their geometry and quality and then optimized (*SI Appendix*, Fig. S9). To further explore the potential binding mode of D4, we performed a binding site search protocol to identify cavities or potential binding sites on the proteins. Molecular docking indicates that D4 could bind in a region delimited by N-terminal helix (NTH), transmembrane helix 1 (TMH1), TMH2 of one protomer, and the TMH1 from a neighbor protomer under the NTH of mCx43 HC (Fig. 5*A*), with a high estimated binding affinity ($\Delta G = -10.83$ kcal/mol). One pocket accommodates the quinoline ring through aromatic and van der Waals interaction with Phe30 in TMH1 and the aliphatic side chains of Asp12 in NTH, Ser27, and Ile31in TMH1 and Thr89 in TMH2. A second pocket interacts with the benzoyl moiety, which is accommodated with the side chains of Ile82, Ile83, and Leu35 on the adjacent protomer, and a third pocket that accommodates the remaining phenyl group comprised by the side chains of residues Ile83, Val87, and Leu90 in THM2, Ile31 and Leu35 on the adjacent TMH1. A characteristic H-bond interaction pattern occurs between Ser86 and the nitrogen atom of the quinoline ring, the oxygen atom of the ester group, and the carbonyl group of the benzoyl moiety of D4.

This pocket is absent in the mCx43 GJC, and D4 is predicted to bind over the NTH in a crevice limited by TMH3 and TMH1 from the adjacent protomer (Fig. 5*B*). The predicted binding mode shows a lower predicted binding affinity ($\Delta G = -8.71$ kcal/mol) and involves and hydrogen bond interaction between the side chain of Ser27 and the quinoline ring, which is also packed with aliphatic side chains of Val24 in the

same TMH1, Leu91 and Ala94 in adjacent TMH3, the phenyl group interacts with aromatic Phe97, and the side chain of Leu93, while the 4-chlorobenzoyl establishes aliphatic interactions with the side chains of Ala6 and Leu10 in NTH.

In the case of mCx39 HC, D4 is predicted to bind under the NTH with lower binding affinity as calculated for mCx43 ($\Delta G = -7.19$ kcal/mol) and a different binding mode (Fig. 5*C*), with the quinoline ring flanked by hydrophobic part of the side chains of residues Leu-3 and Leu-6 in NTH and Glu28, Val29, Arg32, and Met33 in TMH1. The phenyl group is accommodated with the side chains of Leu3 in NTH and Val37 and Met33 in TMH1. Finally, the benzoyl group establishes a hydrogen bond interaction with the amine group in Glu1 and aliphatic interactions with the side chains of Leu74 and Leu78 in TMH3. A second potential binding site located in the extracellular region within the extracellular loops 1 and 2 (Fig. 5*D*) can also accommodate D4 with a similar binding affinity ($\Delta G = -7.85$ kcal/mol). In this binding mode, D4 establishes a hydrogen bond through its carbonyl groups of the ester moiety and the side chain of Ser69, the phenyl ring establishes aromatic interactions with Phe51 and Tyr65, the benzoyl group is flanked by the side chains of Pro73, Phe142, and Ile175, while the quinoline ring orients toward the solvent and establishes aromatic π-stacking interaction with Phe68 and aliphatic interactions with the side chains of Val146, Val150, and Val165. Noteworthy, superimposition of mCx43 HC with best docking results for D4 and mCx43 GJC (Fig. 5*E*) shows that the benzoyl, phenyl, and quinolone aromatic moieties present in D4 spatially overlap with the side chain of residues Trp4, Leu-7, and Leu11 in the mCx43 GJC conformation. These in silico simulations offer an explanation for the preferential binding of D4 to Cx43 HCs but not Cx43 GJs or Cx39 HCs.

Discussion

Accumulating evidence showed the potential of Cx HCs as targets for epilepsy treatment. Here, we demonstrate the prolonged effects of D4 as an HC blocker on neuroinflammation and hyperexcitability in the pilocarpine-induced SE model. Preapplication of D4 strongly reduces glial activation and altered neuronal excitability induced by pilocarpine. Postepileptic treatment with D4 reverts glial activation, normalized neuroinflammation, and levels of mRNA of neuroinflammatory and synaptic genes. Furthermore, D4 inhibits astrocytic HC activity in epileptic animals in two regions of the brain (APC and hippocampus). Overall, our findings indicate that Cx HC inhibition by D4 is a promising strategy in epilepsy treatment.

Blockers of Cx-based GJCs and HCs have provided a great tool to study the role of Cxs in epilepsy by in vivo and in vitro pharmacological intervention. The anticonvulsant effects of nonspecific blockers such as carbenoxolone and quinine, which block not only Cx HCs and GJCs, but also other ion channels or neurotransmitter systems in different in vivo and in vitro epilepsy models (32–43). Cx-mimetic peptides such as Gap 27, which binds to both Cx HCs and GJCs, attenuated spontaneous epileptiform activity in organotypic hippocampal slice cultures (44). Application of peptide 5, a Cx43-mimetic peptide blocker, at low concentration protects neurons in hippocampal slices (45). TAT-Gap 19, a selective Cx43 HC blocker (27), suppressed seizure activity and decreased the concentration of D-serine, which promotes neuronal excitability by modulating NMDA receptors. Because GJCs are responsible for vital functions such as metabolic and electrical communication between assemblies of astrocytes, neurons, or cardiomyocytes and Cx HCs are not permanently active, Cx HCs can serve as a good target for epilepsy treatment with fewer side effects (9). While a previous study examined the effect of TAT Gap 19 on acute seizure activity during pilocarpine perfusion into the hippocampus (27), our study focused on the effect of D4 on prolonged neuroinflammation and hyperexcitability. Although we did not evaluate the functional state of astrocytic GJCs after pilocarpine, it is likely that both reduction in gap junctional communication and increase HC activity contribute to the pathology of epilepsy and seizure (46). In this study, we show that D4 strongly reduces the pilocarpine-induced activation of astrocytes and microglia and astrocytic HC activity, corroborating and extending the results reported using TAT Gap 19 in epilepsy (27).

A great advantage of D4 is how it is delivered into the body. Previous drugs that target Cxs are delivered to the animal either by direct administration into the brain, e.g., CBX into the motor cortex or entorhinal cortex (32, 34), or quinine into the entorhinal cortex (40) or by intraperitoneal injection [e.g., CBX and TAT Gap 19 (27, 47)]. In contrast, our Cx HC blocker D4 was delivered by oral gavage, which is similar to oral administration and is the most common way by which people take medications. After oral gavage, D4 travels from the stomach into the circulation system to all parts of the body. One important issue is whether D4 can penetrate the brain–blood barrier (BBB) into the CNS. The CNS is shielded from the peripheral immune response by the BBB, which consists of three cellular elements of the brain microvasculature, including endothelial cells, astrocyte end-feet, and pericytes (47). Up-regulation of inflammatory mediators by peripheral and central inflammation promotes BBB permeability through multiple mechanisms in epilepsy (47). Although we did not test the bioavailability of D4 in the circulation system and CNS, it is possible that BBB breakdown after pilocarpine-induced SE (48) could facilitate D4 entry into the CNS. Additionally, one unsolved question is whether D4 itself or its metabolite(s) contributes to the antiepileptic effect in the pilocarpine epilepsy model. More in-depth investigation on how D4 penetrates the brain and how its metabolite(s) mediates its anticonvulsant effects in vivo should be conducted in the future.

D4 is a computationally designed, selective Cx HC blocker that does not affect the coupling of adjacent cells (29). D4 has been demonstrated to inhibit Cx43 HCs while not affecting Cx39 HCs and Cx43 GJCs (29). Although several solved Cx structures have been reported in recent years (49, 50), for mCx43 and mCx39, no structure has been reported to date. Our docking simulation suggested that D4 binds preferentially in a region under the NTH limited also by TMH1 and TMH2 of one protomer and the TMH1 of the adjacent protomer. The proposed binding mode may explain the selective blockade of mCx43 HCs and not GJCs, by means of a restricted movement of NTH that can impede channel opening. The obtained binding mode of D4 to the mCx43 GJC will not affect pore diameter or the movement of molecules through the channel. Similarly, binding of D4 to mCx39 HC in both binding sites is predicted to have only a mild effect on HC transport activity. Cx39 belongs to the delta family of Cxs that does not have a conserved tryptophan residue in the NTH (51), and the binding to the secondary pocket is not expected to generate large conformational changes or alter Cx43 GJCs.

Cx HCs in their open state are permeable to the fluorescent dye CBF and other molecules with low molecular weight (<376 Da) (52). Consistent with previous studies (53), our results showed that CBF uptake is weak in the control brain

slices and dramatically increases upon exposure to DCFS or pilocarpine, suggesting that CBF uptake is a good indicator for Cx HC activity in brain slices. We showed that CBF uptake was strongly reduced by D4 in epileptic slices in both GFAP-positive and -negative cells. Uptake in GFAP-negative cells likely occurs in neurons in response to Cx HC activity in glial cells causing the release of glutamate and ATP that can activate neuronal pannexin1 HCs, as demonstrated previously using toxic β-amyloid peptide as inflammatory agent (24). Our previous study examined the effect of D4 on Cx39 HC, Cx45 HC, Cx43 HC, and Cx43 GJCs in heterologous cells transfected with corresponding Cx protein (29). Here, we show that D4 also blocks Cx26 and Cx30 HCs, which can be coexpressed with Cx43 in astrocytes (11), suggesting that all astroglial Cx HC found in different brain regions are inhibited by D4.

Neuroinflammation is a chronic response to pathological conditions such as tissue damage, stress, infection, and seizures (54). Events associated with neuroinflammation include the release of inflammatory molecules such as cytokines and chemokines, release of danger signals such as ATP, activation of astrocytes and microglia, breakdown of BBB, and generation of reactive oxygen species (ROS) and reactive nitrogen species(54, 55). Under pathological conditions, gliotransmitters such as glutamate and ATP released from Cx HCs can facilitate inflammatory response and trigger neuronal damage (16, 22, 25). In addition, the release of ROS or proinflammatory cytokines such as tumor necrosis factor (TNF)-α and interleukin 1β will further activate Cx HCs, forming a vicious positive feedback loop with neuroinflammation (25, 56). D4 breaks this vicious positive feedback loop by blocking Cx HCs, where the release of gliotransmitters is decreased and neuroinflammation is also suppressed correspondingly. Interestingly, we found that, in the hippocampus, preapplication of D4 can suppress microglia (Iba1) but not astrocyte (GFAP) activation, while postapplication can afford the suppression of both glial populations (Fig. 1). Additionally, in the APC, both pre- and postapplication of D4 afforded the suppression of astrocytic activation (Fig. 1). It is unclear how astrocyte vs. microglia activation depends on the timing of Cx HC activity relative to SE. A recent report suggests that microglia are first activated, which, in turn, activates the astrocytes (57). However, we did not find that the astrocytic or microglial gene expression precedes one or the other (Fig. 3). It is possible that we did not have the temporal resolution to discern the fine temporal sequence of astrocytic vs. microglial gene regulation. One potential scenario is that preapplication curbs HC activation during SE, while postapplication curbs HC activation in the few hours after SE. A possible explanation is that astrocyte activation in the hippocampus requires HC activation during SE, while astrocytes in the APC require HC activation after SE. It is also possible that the sequence of astrocytic vs. microglial activation depends on the seizure model and regimen of induction. We demonstrated that D4 posttreatment broadly decreased mRNA levels of neuroinflammatory factors related to astrocyte activation, microglia activation, proinflammatory cytokines, and inflammasome in epileptic animals after a prolonged period (7 d). Consistent with this, mRNA levels of synaptic proteins were increased with D4 posttreatment compared to the pilocarpine group, suggesting less synaptic loss. These results suggest that D4 inhibits the activity of Cx HCs, thereby alleviating damage and neuroinflammation.

The most prevalent subtype of Cx HC is Cx43 in the astrocytes, although lower levels of Cx30 and Cx26 can be present in the hippocampus and APC and allow CBF uptake. We showed that D4 (10 μM) can largely block Cx HC activity in brain slices (Fig. 4) and that D4 (1 μM) can also partially block heterologously expressed Cx30 or Cx26 HCs (*SI Appendix*, Fig. S8). It is possible that opening of Cx43 HCs leads to the secondary activation of Cx26 and/or Cx30 HCs in glia. Also, it is possible that Cx26 and Cx30 form heteromeric HCs in astrocytes (58) and D4 can also block them. The concentration of D4 that inhibits response by 50% of D4 for the various Cx HCs in brain slices and in vivo are not known. Future studies are required to determine the specificity and efficacy of D4 against the different subtypes of Cx HCs in the intact brain circuitry, as well as the pharmacodynamics and pharmacokinetics of D4. Other nonselective membrane channels, such as Panx1 HCs and P2X7 receptors, have been shown to play a relevant role in epilepsy (1). Since inhibition of any of these membrane pathways renders significant protection, it is possible that they might be part of a common positive feedback loop, in which a reduced extracellular Ca^{2+} concentration caused by the high neuronal activity increases the activity of at least some of these membrane channels such as Cx HCs and P2X7 receptors (1, 25). Moreover, the elevated intracellular free-Ca^{2+} concentration increase the activity of Panx1 and Cx HCs allowing the release of ATP that causes a persistent activation of P2X7 receptors further contributing to increase the Ca^{2+} inflow (1).

Taken together, we provide evidence showing that the Cx HC blocker D4 exerts potent anticonvulsive effects in the pilocarpine epilepsy model. D4 abrogates the increase in HC activity, leading to recovery of tissue homeostasis following pilocarpine-induced epilepsy. Since D4 targets Cx HCs but not GJCs, we believe that it serves as a specific and effective medication for epilepsy treatment.

Materials and Methods

The Pilocarpine Model of TLE. Both male and female mice of wild-type strain (C57BL6/J) were used in this study. All work was done in accordance with guidelines from the Animal Research Ethics Sub-Committees of the City University of Hong Kong and the Department of the Health of Hong Kong SAR government. Mice were treated with pilocarpine (200 to 300 mg/kg i.p.; Sigma) to induce SE. Diazepam (10 mg/kg i.p., Pamlin; Ceva) was administered 2 h after the onset of SE to stop seizures.

D4 Drug. The chemical compound D4, (*R*)-2-(4-chlorophenyl)-2-oxo-1-phenylethyl quinoline-2-carboxylate, was synthesized using a series of chiral synthetic methods (molecular weight 401.85 g.mol–1) (Qianyan Shenzhen Pharmatech). For in vivo experiments, D4 was dissolved in 100% ethanol as stock (20 mg/mL) and diluted with 0.9% sterile saline to the desired dosage (5, 10, or 20 mg/kg body weight) right before use. Mice were administered 1) D4 by oral gavage 6 h before or 5 h, 1 d, or 2 d after pilocarpine; 2) no gavage control; or 3) vehicle control (10% ethanol in 0.9% sterile saline) as indicated. For ex vivo dye loading experiments, D4 was dissolved in chilled ACSF containing 10% ethanol. Mice were randomly grouped in these experiments.

Immunofluorescent Staining. Mice were deeply anesthetized with a ketamine/xylazine mix (100 mg/kg ketamine and 19 mg/kg xylazine) prior to fixation with 4% paraformaldehyde (PFA) in a 0.1 M phosphate-buffered solution (PBS; pH 7.4; 4 °C) following an initial flush with ice-cold 0.1 M PB. Brains were post-fixed overnight at 4 °C in PFA and cut into 50 μm thick coronal sections in 0.1 M PB using Leica vibratome (VT1000 S). Then sections were incubated for 1 h with blocking solution (5% normal goat serum, 1% Triton X-100 in PBS) before incubation overnight at 4 °C with primary antibodies in blocking solution (rabbit anti-GFAP antibody [Dako, GA524, 1:1,000]; rabbit anti-Iba1 antibody [Wako, 019-19741, 1:1,000]). Sections were washed 3 × 10 min with PBS at room temperature (RT) and incubated for 1 h at RT in secondary antibodies (anti-rabbit or anti-mouse immunoglobulin G–conjugated Alexa Fluorochrome [Jackson Immunoresearch; 1:1,000], DAPI [Jackson Immunoresearch, SAC-ac-3598, 1:10,000]). Sections were washed 3 × 10 min with PBS at RT. The stained sections were mounted using VECTASHIELD Antifade Mounting Medium on slides

and imaged using Zeiss LSM 880 Confocal Microscope with Zeiss imaging software. Images of the APC and hippocampus were acquired with a 20× objective lens.

Image Analysis. GFAP or Iba1 expression covered area percentage and mean intensity level were quantified using Fiji–ImageJ analyzing tool (Analyze\Measure) after filtering background noise (Image\Adjust\Threshold). A minimum threshold was chosen to exclude background and include structures that appear with astrocytic or microglial morphology after measuring the gray value of background and target. The maximal threshold was left at a maximum (255 for 8-bit images). The threshold was determined for each protein individually and kept constant for different experimental conditions.

RNA Isolation and qPCR. Total RNA from the APC and hippocampus was extracted and isolated by TaKaRa MiniBEST Universal RNA Extraction Kit (catalog no. 9767) according to the manufacturer's instructions. For all sample types, 1 μg of total RNA was used for complementary DNA synthesis with TaKaRa PrimeScript RT Master Mix (Perfect Real Time; catalog no. RR036A), and qRT-PCR was performed with Fast SYBR-Green Master Mix (Applied Biosystems) detected by StepOnePlus Real-Time PCR system (Applied Biosystems). The sequences of qPCR primers used for mRNA quantification in this study were obtained from Primer Bank and are shown in Table1.

After 40 cycles, the Ct values were determined. To normalize the samples, ΔCt between target genes and GAPDH was calculated. The x-fold difference in expression between control, epileptic and rescue samples was then determined by subtraction of the ΔCt values and termed ΔΔCt. Finally, the total change was calculated as $2^{-\Delta\Delta ct}$ and the relative amount in occluded side compared with open side was deducted.

Dye Uptake. For dye uptake in brain slices, coronal slices of the hippocampus were prepared as in *Whole-Cell Patch-Clamp Electrophysiology*. Acute slices were incubated with 10 μM D4 for 30 min in a chamber oxygenated by bubbling gas mixture (95% O_2 and 5% CO_2) into ACSF, pH 7.4 (59). Fifteen minutes after applying D4, 100 μM CBF (Sigma 21877; molecular weight 376.3 g·mol^{-1}) was added into ACSF. Fifteen minutes after applying CBF, slices were then washed five times with ACSF, fixed at RT with 4% PFA overnight at 4 °C, then kept in 30% sucrose for 2 d for cryoprotection. Slices were then frozen in optimal cutting temperature compound (OCT) and dissected in 20- to 30-μm-thick sections with a cryostat (Leica). The sections were then mounted in Fluoromount (Thermo Fisher) and incubated in 0.1% PBS–Triton X-100 containing 10% normal goat serum for 1 h. Then, sections were incubated overnight at 4 °C with either rabbit anti-GFAP antibody (GA524, 1:1,000; Dako) to detect astrocytes. Secondary staining and image acquisition were performed as described above.

The overall CBF covered area percentage and mean intensity level were quantified using Fiji–ImageJ analyzing tool (Analyze\Measure) after filtering background noise (Image\Adjust\Threshold). A minimum threshold was chosen to exclude background and include structures that appears to be neuropils or neuronal/glial cells after measuring the gray value of background and target. The maximal threshold was left at a maximum (255 for 8-bit images). CBF area percentages in astrocytes were quantified with GFAP-positive cells. ROI of astrocyte expression was cropped using the Fiji–ImageJ editing tool (Edit/Selection/Create selection) after filtering background noise (Image\Adjust\Threshold). CBF area percentage in ROI of astrocyte was quantified using the FIJI-ImageJ analyzing tool (Analyze\Analyze Particles) after filtering background noise (Image\Adjust\Threshold).

For dye uptake in heterologous cells, HeLa cells transfected with mCx30 or mCx26 were used (kind donation from Christian Giaume, College de France, Paris, France and Klaus Willecke, Life and Medical Sciences Institute, Molecular Genetics, University of Bonn, Bonn, Germany, respectively). The functional state of Cx HCs was evaluated by DAPI uptake that fluoresces upon binding to nucleic acids of cells. HeLa cells were incubated in Krebs solution containing (in millimolar) 118 NaCl, 4.7 KCl, 3 $CaCl_2$, 1.18 $MgCl_2$, 10 glucose, 20 Hepes, and 9.9 Tris, pH 7.4. Then, cells were exposed to DCFS (same composition as Krebs but without $CaCl_2$ and $MgCl_2$), followed by 1 μM D4 and finally 200 μM La^{3+}. Time-lapse fluorescence snapshot images were taken every 15 s. The DAPI fluorescence was recorded in regions of interest using a Nikon Eclipse Ti microscope.

Whole-Cell Patch-Clamp Electrophysiology. Coronal slices of the hippocampus were prepared in ice-cold slicing solution containing (in millimolar) 110 choline-Cl, 2.5 KCl, 0.5 $CaCl_2$, 10 $MgSO_4$, 1.25 NaH_2PO_4, 24 $NaHCO_3$, and 20 glucose. Following a recovery period of 1 h at RT, recordings were performed in ACSF containing 119 NaCl, 2.5 KCl, 2.5 $CaCl_2$, 1.3 $MgSO_4$, 1 NaH_2PO4, 26.2 $NaHCO_3$, and 22 glucose that is saturated with 95% O2 and 5% CO_2 (carbogen) unless stated otherwise. Recording pipettes were pulled from borosilicate glass (Harvard Apparatus) and open-tip resistance was typically 3 to 5 MΩ. Recordings were obtained from neurons using the whole-cell patch-clamp technique with an internal solution that was based on Cs+ gluconate (in millimolar): 130 D-gluconic acid, 130 CsOH, 5 NaCl, 10 Hepes, 12 Di-Tris-P-creatine, 1 EGTA, 3 Mg-ATP, and 0.2 Na-GTP (pH 7.3; 290 mOsm). For recordings of IPSCs, cells were held at holding potentials (Vh) of +10 mV. sIPSC amplitude and frequency were analyzed using custom-written scripts in MATLAB (MathWorks).

LFP recording in acute pilocarpine model. Awake mice were administrated with pilocarpine (200 to 250 mg/kg) by intraperitoneal injection. After 1 h, mice were anesthetized by ketamine–xylazine solution (100 mg/kg of ketamine and 10 mg/kg of xylazine in saline) when they were in SE. A craniotomy was stereotaxically made on each of the bilateral primary motor cortex (AP +1.2, ML ±1.8 mm relative to bregma) and a single electrode (Tungsten Microelectrode, FHC) was lowered to each primary motor cortex (DV −1 mm) for LFP recording. After 10 min of recording, the electrodes were moved away and D4 (5 to 20 mg/kg) was administrated by oral gavage. Then, the electrodes were stereotaxically implanted again at the same location for another 10-min LFP recording. LFP recordings were acquired by a two-channel amplifier (model 1800; A-M Systems) at a gain of 100 and filter settings of between 0.1 Hz and 2 kHz. Signals were sampled at a 20 kHz sampling rate, digitized by a DAQ board (National Instruments) and recorded with WaveSurfer in MATLAB (https://wavesurfer.janelia.org/).

Table 1. Primer pairs used for qRT-PCR analysis of inflammatory and neuronal genes

Primer	Forward	Reverse
Gapdh	AGGTCGGTGTGAACGGATTTG	TGTAGACCATGTAGTTGAGGTCA
Pvalb	ATCAAGAAGGCGATAGGAGCC	GGCCAGAAGCGTCTTTGTT
homer1	CCCTCTCTCATGCTAGTTCAGC	GCACAGCGTTTGCTTGACT
Tnfa	TAGCTCCCAGAAAAGCAAGCA	CCATCTTTTGGGGGAGTGCC
Gad1	CTTCTTCAGGCTCTCCCGTG	GTATTAGGATCCGCTCCCGC
vglut1	CAGCCCGCCTACTTTGAAGA	GTGACGACTGCGCAAAAAGT
tnfr1	GCTGTTGCCCCTGGTTATCT	ATGGAGTAGACTTCGGGCCT
Gfap	CAGATCCGAGAAACCAGCCT	ACACCTCACATCACCACGTC
cd68	GGGGCTCTTGGGAACTACAC	GTACCGTCACAACCTCCCTG
trem2	CTGGAACCGTCACCATCACTC	CGAAACTCGATGACTCCTCGG
c3	CCAGCTCCCCATTAGCTCTG	GCACTTGCCTCTTTAGGAAGTC
cx43	ACAGCGGTTGAGTCAGCTTG	GAGAGATGGGGAAGGACTTGT
nlrp3	ATTACCCGCCCGAGAAAGG	TCGCAGCAAAGATCCACACAG
cx3cr1	GAGTATGACGATTCTGCTGAGG	CAGACCGAACGTGAAGACGAG
tlr9	ATGGTTCTCCGTCGAAGGACT	GAGGCTTCAGCTCACAGGG

LFP Analysis. The data were first preprocessed by downsampling and baseline correction and bandpass-filtered from 1 to 100 Hz. Five segments of 5-s LFP data were randomly picked up from each channel of each animal for spectral power analysis. The Findpeaks function built in MATLAB was applied to detect epileptic spikes. Spikes above twice the threshold value were defined as epileptic spikes. The threshold value was identified by visual inspection of each channel, which did not vary largely.

Molecular Modeling of mCx43 HC/GJC and mCx39 HC Interactions with D4. Protein models for mCx43 residues 2 to 235 (UniProt P23242), and mCx39 residues 1 to 200 (UniProt P23242) were generated using the structures of human Cx26 HC and ovine Cx46/Cx50 GJCs (Protein Data Bank IDs 2ZW3, 7JKC, and 7JJP, respectively) as templates. Modeler v9.2 was used to generate the comparative models of mCx43 HC, mCx43 GJC, and mCx39 HC. One hundred models were obtained for each oligomer (hexamer or and the best model according to Modeler's PDF and DOPE scores was retained. The validation of the structures was performed using the SAVES server (https://saves.mbi.ucla.edu/). The obtained models were sequentially energy-minimized using the steepest descent with backbone atoms fixed and a force constant of 5 for the side chains restraint, and further minimization using the conjugate gradient algorithm with backbone atoms restrained with a force constant of 10.5, and finally no restraints. A dielectric constant of 4 was used to mimic the membrane environment. Minimization runs by up to 30,000 steps or convergence criteria of 0.001 Å kcal/mol for the root mean square (RMS) of the energy gradient.

D4 was drawn, standardized, and saved as an SDF file using MarvinSketch v22.9 (ChemAxon, https://www.chemaxon.com). Conformer generation was performed using OMEGA v4.1.0.0 (OpenEye Scientific Software). QUACPAC v2.1.1.0 (OpenEye Scientific Software) was used to assign AM1BCC charges to the D4 conformer library. The binding sites of mCx43 HC, mCx43 GJC, and mCx39 HC were identified and prepared using Make Receptor v4.0.0.0 (OpenEye Scientific Software). The candidate binding modes of D4 within the receptor sites were obtained and optimized by using the Chemgauss4 scoring function. Each binding mode of D4 with the different binding sites was minimized with the CHARMm22 force field available in Discovery Studio v2.1 (Accelrys Inc.). The protocol allows minimizing the side chains of residues within 6 Å from the center of mass of all D4 binding modes, using the conjugate gradient algorithm up to a convergence criterion of 0.001 Å kcal/mol for the RMS of the energy gradient. A final evaluation of the binding energy was performed for each obtained complex by using the PLP, LigScore, PMF, and LUDI scoring functions. Graphical representations of D4 binding modes were generated using PyMOL (PyMOL Molecular Graphics System, Version 2.5.2; Schrödinger, LLC).

Statistical Tests. A two-sided *t* test (normal data) or two-sided Mann–Whitney *U* test (nonnormal data) was used to denote significant differences between two experimental groups. To compare three different groups, one-way ANOVA followed by Tukey's multiple comparisons post hoc test (normal data) or independent-samples Kruskal–Wallis test (nonnormal data) (significance values were adjusted by the Bonferroni correction) was used. Thresholds for significance were indicated as $*P < 0.05$, $**P < 0.01$, and $***P < 0.001$. The details of statistical tests and results are shown in the figure legends.

Data, Materials, and Software Availability. All study data are included in the article and/or *SI Appendix*.

ACKNOWLEDGMENTS. This work was supported by the Hong Kong Research Grants Council (RGC/ECS 21103818 to C.G.L. and RGC/GRF 11104320 and 11104521 to C.G.L.), Shenzhen General Basic Research Program (JCYJ20190808182203591 to C.G.L.), a grant from ITF-InnoHK, and internal funds from City University of Hong Kong (to C.G.L.) and Fondo Nacional de Desarrollo Científico y Tecnológico (FONDECYT) grant 1191329 (to J.C.S.), Project P09 from the Centro Interdisciplinario de Neurociencias de Valparaíso (to J.C.S.), and Fondo de Fomento al Desarrollo Científico y Tecnológico (FONDEF) project D07I1086 (to J.C.S.).

Author affiliations: [a]Department of Neuroscience, City University of Hong Kong, Hong Kong, China; [b]Shenzhen Research Institute, City University of Hong Kong, Shenzhen, China; [c]Instituto de Neurociencias, Centro Interdisciplinario de Neurociencias de Valparaíso, Facultad de Ciencias, Universidad de Valparaíso, 2381850 Valparaíso, Chile; and [d]Escuela de Química y Farmacia, Universidad San Sebastián, Providencia 7510157, Santiago, Chile

1. C. García-Rodríguez, I. D. Bravo-Tobar, Y. Duarte, L. C. Barrio, J. C. Sáez, Contribution of non-selective membrane channels and receptors in epilepsy. *Pharmacol. Ther.* **231**, 107980 (2022).
2. M. M. Halassa, T. Fellin, H. Takano, J. H. Dong, P. G. Haydon, Synaptic islands defined by the territory of a single astrocyte. *J. Neurosci.* **27**, 6473–6477 (2007).
3. G. Seifert, C. Steinhäuser, Neuron-astrocyte signaling and epilepsy. *Exp. Neurol.* **244**, 4–10 (2013).
4. M. V. Sofroniew, H. V. Vinters, Astrocytes: Biology and pathology. *Acta Neuropathol.* **119**, 7–35 (2010).
5. A. Bordey, S. A. Lyons, J. J. Hablitz, H. Sontheimer, Electrophysiological characteristics of reactive astrocytes in experimental cortical dysplasia. *J. Neurophysiol.* **85**, 1719–1731 (2001).
6. D. A. Coulter, T. Eid, Astrocytic regulation of glutamate homeostasis in epilepsy. *Glia* **60**, 1215–1226 (2012).
7. G. Carmignoto, P. G. Haydon, Astrocyte calcium signaling and epilepsy. *Glia* **60**, 1227–1233 (2012).
8. J. Wetherington, G. Serrano, R. Dingledine, Astrocytes in the epileptic brain. *Neuron* **58**, 168–178 (2008).
9. R. Schulz *et al.*, Connexin 43 is an emerging therapeutic target in ischemia/reperfusion injury, cardioprotection and neuroprotection. *Pharmacol. Ther.* **153**, 90–106 (2015).
10. L. Medina-Ceja, J. C. Salazar-Sánchez, J. Ortega-Ibarra, A. Morales-Villagrán, Connexins-based hemichannels/channels and their relationship with inflammation, seizures and epilepsy. *Int. J. Mol. Sci.* **20**, 1–17 (2019).
11. C. Giaume, C. C. Naus, J. C. Sáez, L. Leybaert, Glial connexins and pannexins in the healthy and diseased brain. *Physiol. Rev.* **101**, 93–145 (2021).
12. N. Wang *et al.*, Connexin mimetic peptides inhibit Cx43 hemichannel opening triggered by voltage and intracellular Ca2+ elevation. *Basic Res. Cardiol.* **107**, 304 (2012).
13. J. C. Sáez, V. M. Berthoud, M. C. Brañes, A. D. Martínez, E. C. Beyer, Plasma membrane channels formed by connexins: Their regulation and functions. *Physiol. Rev.* **83**, 1359–1400 (2003).
14. C. Giaume, M. Theis, Pharmacological and genetic approaches to study connexin-mediated channels in glial cells of the central nervous system. *Brain Res. Brain Res. Rev.* **63**, 160–176 (2010).
15. K. Shintani-Ishida, K. Uemura, K. Yoshida, Hemichannels in cardiomyocytes open transiently during ischemia and contribute to reperfusion injury following brief ischemia. *Am. J. Physiol. Heart Circ. Physiol.* **293**, H1714–H1720 (2007).
16. T. C. Clarke, O. J. S. Williams, P. E. M. Martin, W. H. Evans, ATP release by cardiac myocytes in a simulated ischaemia model: Inhibition by a connexin mimetic and enhancement by an antiarrhythmic peptide. *Eur. J. Pharmacol.* **605**, 9–14 (2009).
17. M. A. Retamal, K. A. Schalper, K. F. Shoji, M. V. L. Bennett, J. C. Sáez, Opening of connexin 43 hemichannels is increased by lowering intracellular redox potential. *Proc. Natl. Acad. Sci. U.S.A.* **104**, 8322–8327 (2007).
18. X. Bao, G. A. Altenberg, L. Reuss, Mechanism of regulation of the gap junction protein connexin 43 by protein kinase C-mediated phosphorylation. *Am. J. Physiol. Cell Physiol.* **286**, C647–C654 (2004).
19. M. A. Retamal, C. J. Cortés, L. Reuss, M. V. L. Bennett, J. C. Sáez, S-nitrosylation and permeation through connexin 43 hemichannels in astrocytes: Induction by oxidant stress and reversal by reducing agents. *Proc. Natl. Acad. Sci. U.S.A.* **103**, 4475–4480 (2006).
20. H. A. Sánchez, J. A. Orellana, V. K. Verselis, J. C. Sáez, Metabolic inhibition increases activity of connexin-32 hemichannels permeable to Ca2+ in transfected HeLa cells. *Am. J. Physiol. Cell Physiol.* **297**, C665–C678 (2009).
21. Z. Ye, M. S. Wyeth, S. Baltan-tekkok, B. R. Ransom, Functional hemichannels in astrocytes: A novel mechanism of glutamate release. *J Neurosci.* **23**, 3588–3596 (2003).
22. C. Meunier *et al.*, Contribution of astroglial Cx43 hemichannels to the modulation of glutamatergic currents by D-serine in the mouse prefrontal cortex. *J. Neurosci.* **37**, 9064–9075 (2017).
23. A. W. Lohman, B. E. Isakson, Differentiating connexin hemichannels and pannexin channels in cellular ATP release. *FEBS Lett.* **588**, 1379–1388 (2014).
24. J. A. Orellana *et al.*, ATP and glutamate released via astroglial connexin 43 hemichannels mediate neuronal death through activation of pannexin 1 hemichannels. *J. Neurochem.* **118**, 826–840 (2011).
25. T. D. Montero, J. A. Orellana, Hemichannels: New pathways for gliotransmitter release. *Neuroscience* **286**, 45–59 (2015).
26. X. Li *et al.*, Inhibition of connexin43 improves functional recovery after ischemic brain injury in neonatal rats. *Glia* **63**, 1553–1567 (2015).
27. L. Walrave *et al.*, Inhibition of astroglial connexin43 hemichannels with TAT-Gap19 exerts anticonvulsant effects in rodents. *Glia* **66**, 1788–1804 (2018).
28. J. A. Orellana, M. A. Retamal, R. Moraga-Amaro, J. Stehberg, Role of astroglial hemichannels and pannexons in memory and neurodegenerative diseases. *Front. Integr. Neurosci.* **10**, 26 (2016).
29. B. A. Cisterna *et al.*, Active acetylcholine receptors prevent the atrophy of skeletal muscles and favor reinnervation. *Nat. Commun.* **11**, 1073 (2020).
30. G. Curia, D. Longo, G. Biagini, R. S. G. Jones, M. Avoli, The pilocarpine model of temporal lobe epilepsy. *J. Neurosci. Methods* **172**, 143–157 (2008).
31. J. A. Cobb *et al.*, Density of GFAP-immunoreactive astrocytes is decreased in left hippocampi in major depressive disorder. *Neuroscience* **316**, 209–220 (2016).
32. L. Medina-Ceja, A. Cordero-Romero, A. Morales-Villagrán, Antiepileptic effect of carbenoxolone on seizures induced by 4-aminopyridine: A study in the rat hippocampus and entorhinal cortex. *Brain Res.* **1187**, 74–81 (2008).
33. M. O. Bostanci, F. Bağirici, Anticonvulsive effects of carbenoxolone on penicillin-induced epileptiform activity: An in vivo study. *Neuropharmacology* **52**, 362–367 (2007).
34. K. E. Nilsen, A. R. C. Kelso, H. R. Cock, Antiepileptic effect of gap-junction blockers in a rat model of refractory focal cortical epilepsy. *Epilepsia* **47**, 1169–1175 (2006).
35. Z. Gajda, Z. Szupera, G. Blazsó, M. Szente, Quinine, a blocker of neuronal Cx36 channels, suppresses seizure activity in rat neocortex in vivo. *Epilepsia* **46**, 1581–1591 (2005).
36. M. Srinivas, M. G. Hopperstad, D. C. Spray, Quinine blocks specific gap junction channel subtypes. *Proc. Natl. Acad. Sci. U.S.A.* **98**, 10942–10947 (2001).

37. A. J. Thompson, S. C. R. Lummis, Antimalarial drugs inhibit human 5-HT(3) and GABA(A) but not GABA(C) receptors. *Br. J. Pharmacol.* **153**, 1686–1696 (2008).
38. L. Zou *et al.*, The effects of quinine on neurophysiological properties of dopaminergic neurons. *Neurotox. Res.* **34**, 62–73 (2018).
39. W. Chen, Z. Gao, Y. Ni, Z. Dai, Carbenoxolone pretreatment and treatment of posttraumatic epilepsy. *Neural Regen. Res.* **8**, 169–176 (2013).
40. L. Medina-Ceja, C. Ventura-Mejía, Differential effects of trimethylamine and quinine on seizures induced by 4-aminopyridine administration in the entorhinal cortex of vigilant rats. *Seizure* **19**, 507–513 (2010).
41. X. Ran *et al.*, Effects of gap junctions blockers on fast ripples and connexin in rat hippocampi after status epilepticus. *Epilepsy Res.* **146**, 28–35 (2018).
42. C. Ventura-Mejía, L. Medina-Ceja, Decreased fast ripples in the hippocampus of rats with spontaneous recurrent seizures treated with carbenoxolone and quinine. *BioMed Res. Int.* **2014**, 282490 (2014).
43. A. Simon *et al.*, Gap junction networks can generate both ripple-like and fast ripple-like oscillations. *Eur. J. Neurosci.* **39**, 46–60 (2014).
44. M. Samoilova, K. Wentlandt, Y. Adamchik, A. A. Velumian, P. L. Carlen, Connexin 43 mimetic peptides inhibit spontaneous epileptiform activity in organotypic hippocampal slice cultures. *Exp. Neurol.* **210**, 762–775 (2008).
45. J. J. Yoon, C. R. Green, S. J. O'Carroll, L. F. B. Nicholson, Dose-dependent protective effect of connexin43 mimetic peptide against neurodegeneration in an ex vivo model of epileptiform lesion. *Epilepsy Res.* **92**, 153–162 (2010).
46. C. Steinhäuser, G. Seifert, P. Bedner, Astrocyte dysfunction in temporal lobe epilepsy: K+ channels and gap junction coupling. *Glia* **60**, 1192–1202 (2012).
47. O. Devinsky, A. Vezzani, S. Najjar, N. C. De Lanerolle, M. A. Rogawski, Glia and epilepsy: excitability and inflammation. *Trends Neurosci.* **36**, 174–184 (2013).
48. N. F. Mendes *et al.*, The blood-brain barrier breakdown during acute phase of the pilocarpine model of epilepsy is dynamic and time-dependent. *Front. Neurol.* **10**, 603 (2019).
49. J. B. Myers *et al.*, Structure of native lens connexin 46/50 intercellular channels by cryo-EM. *Nature* **564**, 372–377 (2018).
50. S. Maeda *et al.*, Structure of the connexin 26 gap junction channel at 3.5 A resolution. *Nature* **458**, 597–602 (2009).
51. F. Villanelo *et al.*, Accessing gap-junction channel structure-function relationships through molecular modeling and simulations. *BMC Cell Biol.* **18** (suppl. 1), 5 (2017).
52. E. A. Turovsky *et al.*, Mechanosensory signaling in astrocytes. *J. Neurosci.* **40**, 9364–9371 (2020).
53. V. Abudara *et al.*, The connexin43 mimetic peptide Gap19 inhibits hemichannels without altering gap junctional communication in astrocytes. *Front. Cell. Neurosci.* **8**, 306 (2014).
54. C. Steinhäuser, M. Grunnet, G. Carmignoto, Crucial role of astrocytes in temporal lobe epilepsy. *Neuroscience* **323**, 157–169 (2016).
55. I. D. Bravo-Tobar, P. Fernández, J. C. Sáez, A. Dagnino-Subiabre, Long-term effects of stress resilience: Hippocampal neuroinflammation and behavioral approach in male rats. *J. Neurosci. Res.* **99**, 2493–2510 (2021).
56. M. A. Retamal *et al.*, Cx43 hemichannels and gap junction channels in astrocytes are regulated oppositely by proinflammatory cytokines released from activated microglia. *J. Neurosci.* **27**, 13781–13792 (2007).
57. F. Sano *et al.*, Reactive astrocyte-driven epileptogenesis is induced by microglia initially activated following status epilepticus. *JCI Insight* **6**, e135391 (2021).
58. S. W. Yum *et al.*, Human connexin26 and connexin30 form functional heteromeric and heterotypic channels. *Am. J. Physiol. Cell Physiol.* **293**, C1032–C1048 (2007).
59. J. A. Orellana *et al.*, Amyloid β-induced death in neurons involves glial and neuronal hemichannels. *J. Neurosci.* **31**, 4962–4977 (2011).